

Clinically inspired enhance Explainability and Interpretability of an AI-Tool for BCC diagnosis based on expert annotation

Iván Matas^a, Carmen Serrano^a, Francisca Silva^b, Amalia Serrano^b, Tomás Toledo-Pastrana^c, Begoña Acha^a

^a*University of Seville, Seville, Spain*

^b*Hospital Universitario Virgen de Macarena, Seville, Spain*

^c*Hospital Quirón Salud Infanta Luisa y Sagrado Corazón, Seville, Spain*

Abstract

Background and Objective: An AI tool has been developed to provide interpretable support for the diagnosis of BCC by teledermatology, thus speeding up referrals and optimizing resource utilization. Dermatologists base their BCC diagnosis on the presence or absence of specific BCC dermoscopic features. Our clinically inspired explainability approach relies on two key pieces of evidence: the BCC dermoscopic patterns identified in the image by the AI classification system and the image regions where the AI tool focuses, which correspond to the presence of BCC patterns.

Methods: A dataset of 1559 dermoscopic images was annotated by several dermatologists. MobileNet-V2 was employed for BCC/non-BCC classification and BCC pattern detection, developing a clinically-inspired XAI approach. The model was trained using stratified cross-validation and data augmentation to address class imbalance. Visual XAI was implemented to validate the clinically-inspired XAI detection. Since there is no established ground truth for BCC dermoscopic features, a standard reference was inferred from the diagnoses of four dermatologists using an algorithm based on expectation maximization (EM).

Results: The results demonstrate significant improvements in classification accuracy and interpretability, positioning this approach as a valuable tool for early BCC detection and referral to dermatologists. The BCC/non-BCC classification achieved an accuracy rate of 90%. For clinically-inspired explainable AI (XAI) results, the detection of BCC patterns useful to clinicians reaches 99% accuracy. As for the Clinically-inspired Visual XAI results, the

mean of the Grad-CAM normalized value within the manually segmented clinical features is 0.57, while outside this region it is 0.16. This indicates that the model struggles to accurately identify the regions of the BCC patterns. These results demonstrate the ability of the AI tool to provide a useful explanation.

Conclusions: Based on these results, two significant clinical achievements have been attended: (1) A tool with dual explanation capabilities rooted in clinical practice has been developed, which improves reliability and adoption by dermatologists. (2) This advancement allows integration into the clinical field, which could change the current protocol in primary care centers to accelerate treatment for patients with BCC lesions in various areas of Andalusia.

Keywords: Basal Cell Carcinoma, Deep Learning, Skin Cancer, Telemedicine, XAI

1. Introduction

Worldwide, doctors diagnose skin cancer most commonly, with Melanoma, Basal Cell Carcinoma (BCC), and Squamous Cell Carcinoma (SCC) as the most prevalent types. BCC accounts for approximately 75% of all skin cancers, making it the most frequent form. It has well-established clinical criteria for its diagnosis, yet there is significant variability in the presence of these clinical criteria between cases [1, 2, 3, 4].

The development of public databases has significantly increased the number of published articles related to automatic detection of skin diseases in recent years [5, 6, 7, 8]. Although these databases are accessible and comprehensive for everyone, the clinical criteria used for diagnosis are not readily available. To develop a tool that is useful from a medical perspective, it is crucial to provide not only classification metrics, but also a detailed diagnosis explaining the detected clinical features, offering a more comprehensive result. In this context, Serrano et al. [9] created a clinically inspired skin lesion classification tool by detecting dermoscopic criteria for BCC.

XAI techniques such as Grad-CAM [10] play a crucial role in improving the transparency and interpretability of CNNs in any kind of medical diagnosis. By offering visual explanations of the decision-making process, these methodologies allow medical professionals to gain insight into the predictive mechanisms of AI models, thus fostering trust and acceptance in AI-driven

diagnoses. The integration of XAI with dermatological applications not only enhances the model’s interpretability but also aids in the early and accurate diagnosis of skin conditions, potentially leading to better patient outcomes. In van der Valden et al. survey [11] there are several works focused on the diagnosis of skin cancer that use different XAI techniques to see how their models behave are explained.

Barata et al. have developed a Computer-Aided Diagnosis (CAD) system based on deep learning for the hierarchical diagnosis of skin lesions, using ISIC 2017 and 2018 datasets. Their model uses attention modules to improve explainability by highlighting important features in dermoscopy images. This approach improves the transparency and interpretability of the diagnostic process, making the system more reliable and suitable for clinical use [12].

Chanda et al. developed a multimodal XAI system to support dermatologists in diagnosing melanoma. Using the HAM10000 dataset, which comprises over 10,000 dermoscopic images, they created a model that provides interpretable, text and region-based explanations alongside its diagnostic predictions. A three-phase reader study involving 116 international dermatologists demonstrated that the XAI system significantly increased clinicians’ trust and confidence in their diagnosis compared to a conventional AI system, although it did not significantly improve diagnostic accuracy [13].

Rezk et al. developed an interpretable skin cancer diagnosis model using clinical images to assist general practitioners in early detection and referral. Their approach incorporates a skin lesion taxonomy into a deep neural network to incrementally learn dermatological concepts. They used a dataset of 914 clinical images, supplemented by additional images from DermNet NZ to address class imbalances. To enhance transparency and trustworthiness in line with recent regulatory requirements, XAI techniques, such as Grad-CAM++, were employed to provide visual explanations of the model’s decisions. The proposed model significantly improved classification accuracy and interpretability, facilitating better understanding and detection of misdiagnoses [14].

However, in [12, 14] works, the use of XAI is employed to visualize the regions where the models have focused to extract features, providing a visual representation of the results returned by the classifier. Besides, [13] introduces a novel use of Grad-CAM to improve dermatologist trust by ensuring the AI model focuses on clinically relevant lesion areas. Grad-CAM explanations are combined with feature detection, aligning AI decisions with expert reasoning, significantly increasing user confidence without sacrificing diagnostic accuracy.

Nevertheless, the key contribution of this work lies in a dual-layer explanation aimed at enhancing clinical diagnosis. Firstly, it offers a binary detection between BCC and non-BCC cases. Secondly, it provides a clinically valuable XAI tool for specialists, enabling them to verify whether its attention is being directed towards the correct BCC-related patterns.

2. Methodology

In modern healthcare, primary care physicians use teledermatology to receive high-quality diagnostic images remotely, allowing preliminary diagnoses of Basal Cell Carcinoma (BCC) using established patterns [4, 15]. Suspected BCC cases are immediately referred to dermatology specialists, improving healthcare efficiency, reducing waiting times, and facilitating early intervention.

Teledermatology is crucial in areas with limited specialist access and its integration with AI tools promises to enhance diagnostic accuracy and efficiency. This work aims to develop an AI tool to assist in this process by providing a binary classification of BCC/non-BCC with interpretable results Fig. 1 illustrates the current and proposed diagnostic workflows. In the proposed workflow, the AI tool not only delivers a BCC/non-BCC diagnosis but also provides a layer of interpretability, guiding the dermatologist to focus on the dermoscopic features most relevant to basal cell carcinoma. This dual-layer explanation ensures that the specialist can validate the AI's predictions by confirming that the model is emphasising the correct clinical patterns, thus reducing the chances of diagnostic errors and increasing trust in AI-assisted teledermatology.

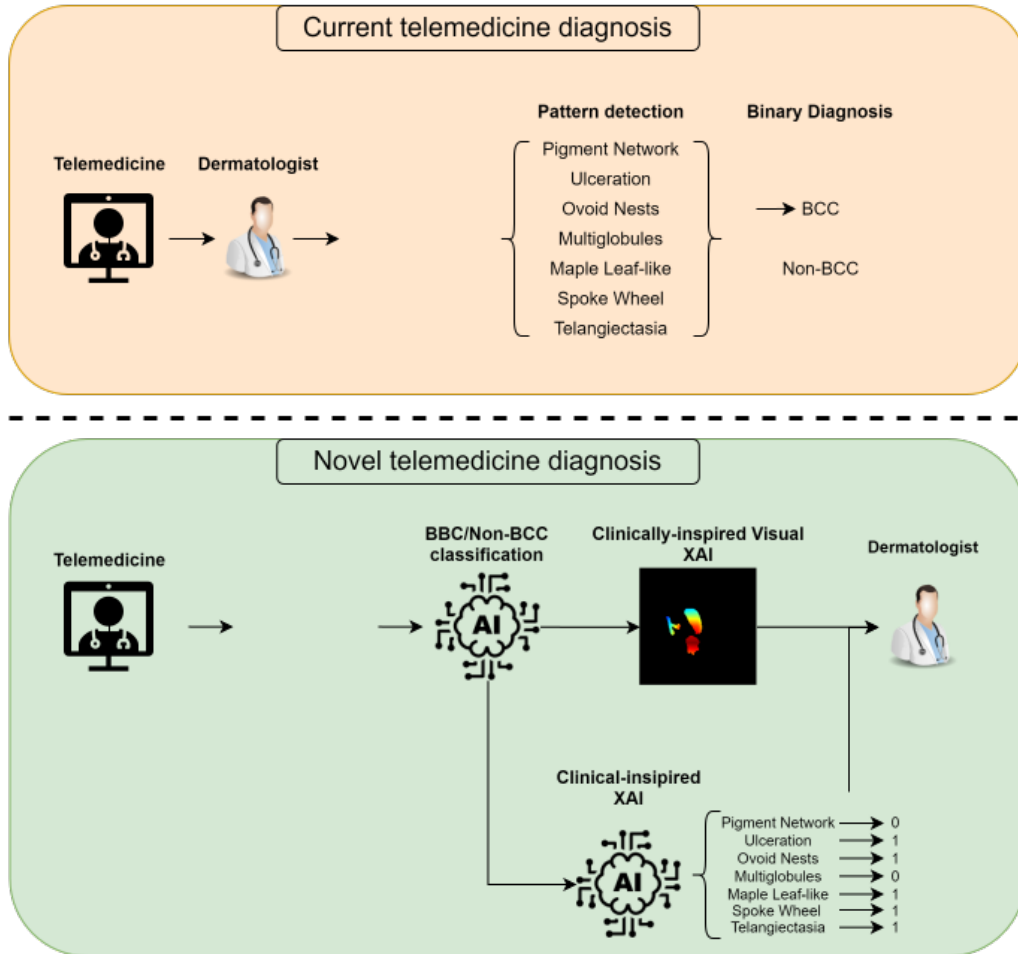


Figure 1: Illustration showing an example of the current workflow of BCC diagnosis by teledermatology in orange and the proposed workflow in green.

2.1. Database

The Dermatology Unit of the “Hospital Universitario Virgen Macarena” provided the entire database, which consists of dermoscopic images sent from 60 primary care centers during 2 years. The dataset comprises 1559 dermoscopic images divided into 3 subsets. Four dermatologists provided different types of annotation according to the subsets. Specifically:

- The first subset consists of 1089 dermoscopic images that were annotated following a multilabel codification explained in Sect. 2.1.1. To consoli-

date the multi-rater labeling, an Expectation-Maximization (EM) algorithm was employed, generating an inferred Standard Reference (SR), which will be explained in Sect. 2.1.2. Subsequently, a binary classification scheme was established to classify into BCC and non-BCC lesions.

- An additional set of 334 images was collected, enriched with detailed dermatological annotations beyond the multilabel and binary SR. It includes specialist’s manual segmentations of the BCC clinical patterns present in a lesion. Several segmented area may appear on an image if there are some patterns in the BCC lesion. In the Fig. 3 an example is shown. These images are designated for the XAI part of the study, enabling a deeper analysis of the model decision process.
- The final subset was gathered from the ISIC Archive [8], utilizing 136 non-BCC images, predominantly consisting of nevus lesions.

2.1.1. Label codification

Each image may contain multiple dermoscopic patterns. Therefore, we used a one-hot coding scheme to encode the labels during image annotation and subsequently process the dermatologists’ annotations. Each image label is a binary word and each BCC dermoscopic pattern is a digit, where 1 means presence and 0 means absence. The seven patterns (Fig. 2) that can appear in a BCC lesion are[4]: Pigment Network (PN) (negative criterion), Ulceration (U), Ovoid Nests (ON), Multiglobules (MG), Maple Leaf-like (ML), Spoke Wheel (SW), Arborizing Telangiectasia (AT). Thus, each label is a vector of dimensions [1x7] using a binary codification where a value of 1 means BCC lesion and a value of 0 means non-BCC lesion. In Table 1 there are some examples of this process.

2.1.2. Standard Reference (SR) Inferring

The accepted ground truth (GT) for BCC diagnosis is biopsy. However, there is no established GT for BCC dermoscopic patterns, which are subjectively assessed by dermatologists. Several studies have reported a low kappa coefficient when measuring inter-dermatologist agreement in determining the different dermoscopic patterns present in a lesion [16, 15]. Therefore, an adequate SR inferred from the consensus of several dermatologists is required. We implemented an Expectation-Maximization (EM) based algorithm [17] to derive a single SR for model training from multiple specialist labels. This

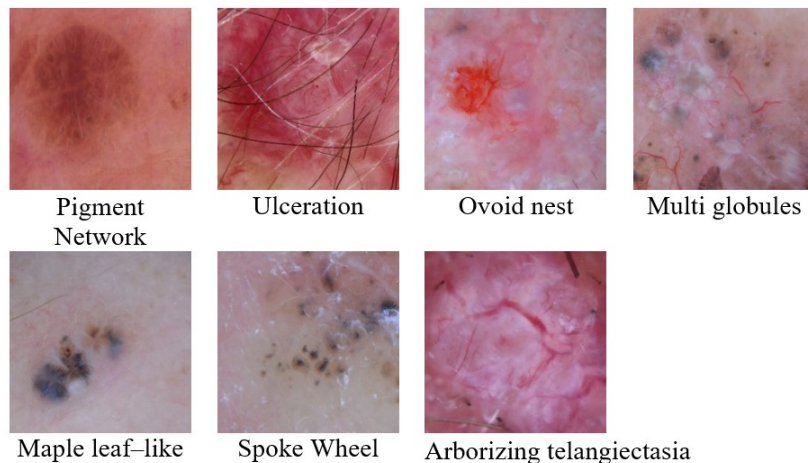


Figure 2: BCC dermoscopic criteria and Pigment Network as a negative criterion.

Table 1: Example of multilabel and binary encoding for BCC diagnosis

Codification	Multi-label	Binary	Diagnosis
Example 1	[0 1 0 1 1 0 1]	1	Presence of BCC
Example 2	[0 0 1 0 0 0 0]	1	Presence of BCC
Example 2	[1 0 0 0 0 0 0]	0	Absence of BCC
Example 3	[0 0 0 0 0 0 0]	0	Absence of BCC

algorithm consolidates multilabel annotations from different dermatologists and generates a single inferred SR that encapsulates the collective expertise of the raters. Silva et al. [18] used this algorithm to infer the SR from BCC pattern annotations and demonstrated that integrating this diverse expertise mitigates the subjectivity inherent in diagnosing the BCC pattern and improves the reliability and robustness of the classification model.

Table 2 summarises the distribution of labels in the database. As can be seen in this table, the database has a significant class imbalance, with SW

Table 2: Sample distribution for binary and multilabel codification.

Binary codification		Multi-label codification						
BCC	Non-BCC	Pigment Network	Ulceration	Ovoid Nests	Multiglobules	Maple Leaf-like	Spoke Wheel	Arborizing Telangiectasia
775	784	557	385	333	191	244	178	455

and MG patterns under-represented. Several techniques have been used to address this problem, see Sect. 3.1.

2.2. Clinically-inspired XAI: BCC diagnosis with additional label information

This section refers to the AI model positioned at the bottom of Novel telemedicine diagnosis in Fig. 1 (Pattern detection AI). From a clinical point of view, achieving 100% accuracy in the detection of dermoscopic BCC patterns is not crucial to a correct diagnosis of BCC. A dermatologist only needs to detect one of the aforementioned BCC patterns to decide whether the lesion is BCC. Therefore, a useful XAI should present the same criterion. The proposed tool presents the following results: if no pattern is detected, it predicts no BCC; if the PN pattern is detected, it serves as a negative criterion, obtaining a prediction of no BCC; and if any other BCC pattern is detected, the prediction is positive for BCC.

The proposed AI tool is based on the MobileNet-V2 model with three classifier layers. The model was coupled with a three-step optimization and training strategy. The first two steps focused on the detection of BCC/non-BCC, while the third step focused on pattern classification. In the first step, ImageNet transfer learning was applied and classifier weights were trained. In the second step, fine-tuning was applied to the last three blocks of the feature extractor, and the classifier was tuned with a lower learning rate (LR) and an increased number of epochs. In the third step, once the column extracts features from the same region as the specialist in the binary task, the classifier was retrained for pattern detection with a very low LR.

In light of the considerable class imbalance evident in Table 2, the methodology was devised to circumvent a direct transition from the adjusted ImageNet weights to patterns characterized by such an imbalance. Instead, an intermediate phase was incorporated, during which the weights were fine-tuned on the dermoscopic images. This intermediate phase allowed the extraction of features specific to dermoscopic images, thereby enhancing the subsequent classification process and ensuring greater accuracy and manageability.

2.3. Clinically-inspired Visual XAI

This section refers to the AI model at the top of Novel telemedicine diagnosis in Fig. 1 (BCC/Non-BCC classification). To develop this concept, expert-generated segmentations are used. As detailed in Sect. 2.1, a subset of samples was segmented by a specialist. A dermatologist performed an individual segmentation of each BCC pattern for each image (Fig. 3).

Understanding the decision-making process of convolutional neural networks (CNNs) is critical for clinical applications where interpretability is as important as performance metrics. The most common visualization techniques in XAI are activation maps and gradient-weighted class activation mapping (Grad-CAM). Activation Maps, as described by Zhou et al. [19], extract features from different network layers to show which patterns the model focuses on, although they may not always directly correlate with specific outcomes. On the other hand, Grad-CAM, as described in detail by Selvaraju et al. [10], uses the gradients of the predicted class that flow into the final convolutional layer to produce a localization map. The clinically-inspired explanation that we proposed in this paper is based on Grad-CAM.

However, additional information for validation is provided. For this study, the segmentations of individual BCC patterns (see 2.1) were combined into a single segmented image, as shown in Fig. 3. The manual segmentations were then overlaid with activation maps to validate the clinical information provided by Grad-CAM. This not only confirmed whether the network is correctly trained in BCC/non-BCC detection, allowing us to use that spine for pattern detection as previously explained, but also identified the dermoscopic pattern of that region verifying if indeed clinical XAI is working correctly.

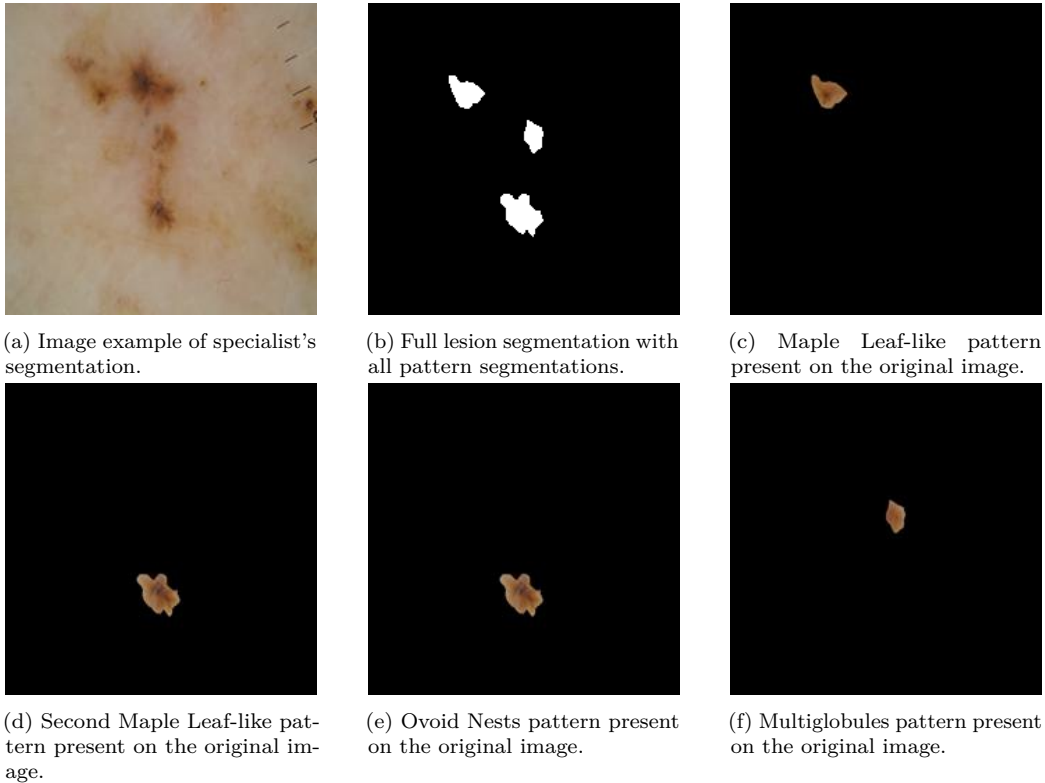


Figure 3: Example of the specialist segmentation job.

3. Results

3.1. Implementation details

Optimisation of the model as a key element of this project. Several critical hyperparameters were carefully adjusted in order to improve performance. The network architecture was trained in two stages. First, ImageNet’s transfer learning stage used the new AdamW schedule-free optimiser [20] with a learning rate of $1e^{-5}$ for 100 epochs, employing a mini-batch size of 32. A dropout rate of 0.3 was established to serve as a regularisation technique to prevent overfitting.

As demonstrated in Sect. 2.1, class imbalance is a significant issue, especially in the multi-label classification of BCC patterns such as ML, MG, or SW. To address this problem, the Focal loss [21] was implemented, which is particularly useful when the distribution of samples is not uniform.

Due to the restricted scope of our database, we have employed a stratified k-fold cross-validation to guarantee a thorough assessment of the model’s efficacy. Specifically, a 5-fold stratification [22, 23] was used, ensuring that each fold was well-representative of the whole dataset, maintaining the proportion of each class in every fold. This approach mitigates the risk of biased training and testing distributions, which is crucial in datasets with imbalanced class distributions.

For the classification model, we chose MobileNet-V2, a lightweight deep neural network known for its efficiency and effectiveness in image classification tasks. To enhance the robustness of the model and account for variabilities in real-world dermoscopic imaging, several data augmentation techniques were applied [24, 25, 26]. These included rotation to mimic variations in the orientation of lesions in clinical images, random perspective to simulate different angles and perspectives from which images can be taken during examinations, and Gaussian blur to represent common issues of slight blur due to patient movement or focus inaccuracies in dermoscopic devices. These augmentation strategies not only help prevent overfitting, but also enhance the model’s ability to generalise to new, unseen images by simulating a variety of imaging conditions in real-world scenarios.

3.2. Clinically-inspired XAI: BCC diagnosis with additional label information

This section analyses the performance of the AI tool for BCC detection in conjunction with the labels provided to explain this classification. Table 3 presents metrics that summarise this performance. The metrics are averaged over all folds. This table has three parts. The first part shows the performance of the AI tool in binary classification. The second part shows its performance in detecting BCC dermoscopic patterns. Finally, the third part represents the accuracy of the labels that provide the clinical explanation.

In general, the diagnostic performance of BCC / non-BCC is high, around 0.9 for all metrics. However, the BCC pattern detection performance needs to be analysed with a deeper insight. Minority classes tend to achieve low recall because the AI tool trained with unbalanced databases tends to favour majority classes. As shown in Sect. 2.1, SW, MG and ML are underrepresented classes. Strategies such as data augmentation and advanced sampling, a one-vs-all strategy combined with stratified k-fold cross-validation helped to achieve a more balanced classification across patterns, thereby improving overall model performance. However, the metrics achieved should not be analysed in the same way as BCC/non-BCC performance. They should

Table 3: Evaluation using binary, multilabel classification metrics and physician-guided analysis.

	Recall (σ^2)	Specificity (σ^2)	Precision (σ^2)	Accuracy (σ^2)
BCC/Non-BCC				
	0.89	0.89	0.90	0.90
Pattern detection				
Pigment Network	0.94 ($4.19 \cdot 10^{-4}$)	0.96 ($1.07 \cdot 10^{-4}$)	0.97 ($2.47 \cdot 10^{-4}$)	0.95 ($4.50 \cdot 10^{-6}$)
Ulceration	0.81 ($4.14 \cdot 10^{-3}$)	0.75 ($8.94 \cdot 10^{-4}$)	0.52 ($8.94 \cdot 10^{-4}$)	0.77 ($4.84 \cdot 10^{-4}$)
OvidNests	0.65 ($2.48 \cdot 10^{-3}$)	0.84 ($1.52 \cdot 10^{-4}$)	0.53 ($3.78 \cdot 10^{-5}$)	0.84 ($1.20 \cdot 10^{-5}$)
Multiglobules	0.61 ($6.16 \cdot 10^{-3}$)	0.81 ($2.05 \cdot 10^{-3}$)	0.32 ($2.15 \cdot 10^{-3}$)	0.80 ($1.10 \cdot 10^{-3}$)
Maple Leaf-like	0.50 ($8.76 \cdot 10^{-3}$)	0.82 ($9.43 \cdot 10^{-5}$)	0.34 ($1.79 \cdot 10^{-3}$)	0.77 ($2.47 \cdot 10^{-4}$)
Spoke Wheel	0.60 ($2.63 \cdot 10^{-3}$)	0.87 ($8.09 \cdot 10^{-4}$)	0.37 ($1.15 \cdot 10^{-3}$)	0.84 ($3.93 \cdot 10^{-4}$)
Arborizing Telangiectasia	0.89 ($1.08 \cdot 10^{-3}$)	0.76 ($4.57 \cdot 10^{-4}$)	0.61 ($4.69 \cdot 10^{-4}$)	0.80 ($2.83 \cdot 10^{-4}$)
Clinically-inspired XAI				
All 0's	-	-	-	0.73
Pigment Network	0.94	0.96	0.97	0.95
BCC pattern detection	0.84	0.88	0.71	0.99

only be evaluated to the extent that they provide a correct explanation for binary classification. For the specialist, a tool that perfectly classifies all BCC patterns within a lesion is not particularly useful, as identifying even a single pattern can already indicate a positive BCC diagnosis. Therefore, the third section of Table 3 provides information relevant to the clinician, highlighting whether there is a BCC pattern detected by the specialist is present. Furthermore, this information is further supported by Table 4, which, as will be discussed later, shows whether the classification of each pattern is being extracted from the same region as identified by the dermatologist. This additional evaluation is summarised in the third section of Table 3, titled ‘‘Clinically-inspired XAI’’. The table demonstrates that 73% of non-BCC lesions without any BCC patterns, 95% of non-BCC lesions with PN, and 99% of BCC lesions with at least one BCC pattern are correctly labelled as such.

3.3. Clinically-inspired Visual XAI

This section aims to quantify the accuracy of the AI tool in focusing on the correct part of the lesion, specifically the BCC dermoscopic patterns identified by clinicians. To this end, the areas of the BCC pattern delineated by dermatologists will be compared with the activated areas of the model. This will provide a quantitative measure of the model’s agreement with human

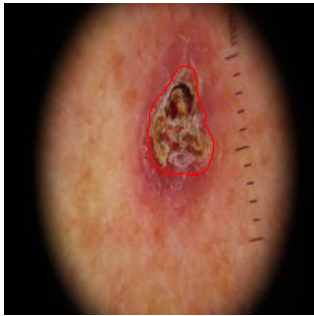
diagnostic criteria and demonstrate its ability to accurately identify critical features of BCC lesions.

To quantify the accuracy of the model activation areas with respect to the areas of clinical interest, the conditional probability density functions of the normalised Grad-CAM values within and outside the area segmented by dermatologist were estimated. Let $z(x, y)$ the Grad-CAM value at position (x, y) . Denote Fg the area segmented by the dermatologist and Bg the background. $P(z(x, y) | \text{Fg})$ is the probability density function of the Grad-CAM values for pixels $(x, y) \in \text{Fg}$ and $P(z(x, y) | \text{Bg})$ is the probability density function of Grad-CAM values for pixels $(x, y) \in \text{Bg}$.

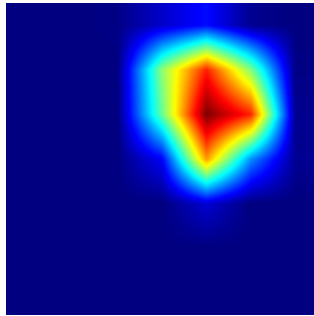
Fig. 4 illustrates this analysis. Fig. 4a shows the original BCC lesion. Fig. 4b shows the Grad-CAM map. Fig. 4c shows the dermatologist’s segmentation overlaid on the Grad-CAM map. Fig. 4d shows an example of the two conditional probability density functions. The orange curve represents $P(z(x, y) | \text{Bg})$, and the blue curve represents $P(z(x, y) | \text{Fg})$. The orange curve is centred near 0, indicating low activation outside the mask, while the blue curve shows significant Grad-CAM information within the clinical segmentation, indicating that the model extracts features from the same region as the specialist.

Table 4 summarises the information extracted from these probability density functions. Specifically, the mean, standard deviation of $z(x, y)$ for $(x, y) \in \text{Fg}$ and $(x, y) \in \text{Bg}$ respectively, and the intersection area between $P(z(x, y) | \text{Fg})$ and $P(z(x, y) | \text{Bg})$ are shown. This table highlights that correctly predicted samples exhibit a higher average $P(z(x, y) | \text{Fg})$ value compared to misclassified samples. In addition, they display a lower average $P(z(x, y) | \text{Bg})$ value, which suggests that the model is focusing on regions akin to those a dermatologist would examine when diagnosing the lesion.

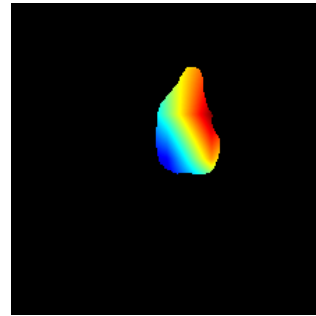
The DICE and Jaccard coefficients are commonly used to evaluate accuracy. However, in this study, these metrics were not applicable due to the significant difference in detail between manual segmentations by specialists and the more generalized regions highlighted by Grad-CAM (Fig. 3). Activation maps tend to cover larger areas than the precise segmentations, making these coefficients less representative for assessing model performance.



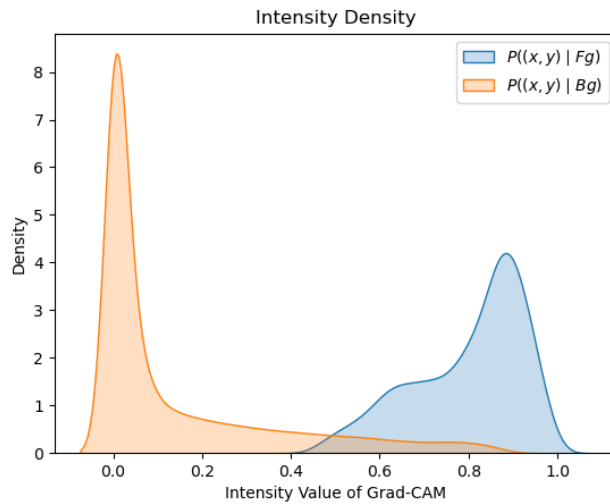
(a) Original image and the detailed BCC pattern segmentation by a specialist in red.



(b) GradCAM heatmap showcasing areas of highest model activation.



(c) Integration of Grad-CAM heatmap and specialist segmentation.



(d) Analysis of Grad-CAM heatmap and expert segmentation. The blue density curve indicates that a significant portion of the Grad-CAM is accurately segmented by the expert.

Figure 4: Demonstration of various interpretative visualizations used in skin lesion analysis, combining expert segmentation and Grad-CAM heatmaps to aid in understanding the model’s decision-making process. This example is from a correct prediction sample.

Table 4: Statistics derived from estimation of conditional probability density functions of Grad-CAM within and outside the region of clinical interest.

Prediction	Intersection	Mean	Mean	Std	Std
		$P(z(x, y) Fg)$	$P(z(x, y) Bg)$	$P(z(x, y) Fg)$	$P(z(x, y) Bg)$
Correct	0.24	0.57	0.16	0.14	0.22
Incorrect	0.32	0.33	0.14	0.01	0.21

4. Discussion

The aim of this work was to develop a tool that is truly useful to dermatologists by incorporating clinically relevant information, such as BCC patterns and their segmentation. The tool provides not only a BCC/non-BCC classification but also a deeper level of interpretability through detailed pattern analysis. However, further refinement is needed to ensure that the tool can deliver not only a binary diagnosis of BCC/non-BCC but also a comprehensive identification of specific patterns with accuracy percentages for each. This level of detail aims to make the information truly valuable for teledermatology applications.

The two essential criteria for the clinical diagnosis of BCC by dermatologists are: (1) the presence or absence of any BCC pattern, and (2) the Pigment Network as a negative criterion. The Clinically-inspired XAI tool correctly detects 99% of cases where any of the six BCC patterns are present in the lesion. Additionally, we aimed to verify that the tool adheres closely to clinical criteria, which is why the double explanation approach was implemented, as illustrated in the results.

As demonstrated in Table 3, the clinical reliability of the diagnosis was confirmed to be robust for specialists. Furthermore, Table 4 indicates that the feature extraction for each dermoscopic pattern was consistently performed from clinically relevant regions, aligning the model’s attention with the areas identified by dermatologists. This alignment validates the model’s ability to not only distinguish between BCC and non-BCC lesions but also to provide precise pattern-based explanations that improve interpretability and clinical trust.

In the literature, there are other studies that have developed tools aimed at addressing similar challenges. Nevertheless, the tool presented in this work uniquely combines BCC/non-BCC detection with an explainability component for BCC patterns, which has been clinically validated as shown in Table 4. This additional layer of clinical interpretability provides a distinctive advantage that existing tools lack, significantly enhancing its value in a medical context.

The implementation of this tool will allow the development of a new primary care protocol in Andalusia, streamlined the workflow between primary care and dermatologists. Its deployment would be highly efficient, as the entire system is built using the lightweight and efficient MobileNet model, which will facilitate this implementation. In addition, its strong clinical

reliability provides a solid foundation for adoption by specialists, ensuring both accuracy and ease of use in clinical settings.

5. Acknowledgements

This work was supported by the Andalusian Regional Government (PROYEX-CEL_00889) and is part of the project of the aid PID2021-127871OB-I00, funded by MCIN/AEI/10.13039/501100011033 and ERDF/European Union (NextGenerationEU/PRTR).

Conflict of Interest Statement

The authors declare that they have no conflict of interest regarding this study.

References

- [1] American Academy of Dermatology, Types of Common Skin Cancer, <https://www.aad.org/public/diseases/skin-cancer/types/common>, accessed: 2024-03-28 (2024).
- [2] Skin Cancer Foundation, Skin Cancer Information, <https://www.skincancer.org/skin-cancer-information>, accessed: 2024-03-28 (2024).
- [3] M. Ciężyńska, J. Narbutt, A. Woźniacka, A. Lesiak, Trends in basal cell carcinoma incidence rates: a 16-year retrospective study of a population in central poland, *Advances in Dermatology and Allergology/Postępy Dermatologii i Alergologii* 35 (1) (2018) 47–52.
- [4] K. Peris, M. C. Fargnoli, C. Garbe, R. Kaufmann, L. Bastholt, N. B. Seguin, V. Bataille, V. Del Marmol, R. Dummer, C. A. Harwood, et al., Diagnosis and treatment of basal cell carcinoma: European consensus-based interdisciplinary guidelines, *European Journal of cancer* 118 (2019) 10–34.
- [5] N. C. F. Codella, D. A. Gutman, M. E. Celebi, B. Helba, M. A. Marchetti, S. W. Dusza, A. Kalloo, K. Liopyris, N. K. Mishra, H. Kittler, A. Halpern, Skin lesion analysis toward melanoma detection: A challenge at the 2017 international symposium on biomedical imaging (isbi), hosted by the international skin imaging collaboration (ISIC), CoRR abs/1710.05006 (2017). [arXiv:1710.05006](https://arxiv.org/abs/1710.05006).
URL <http://arxiv.org/abs/1710.05006>
- [6] M. Combalia, N. C. F. Codella, V. Rotemberg, B. Helba, V. Vilaplana, O. Reiter, C. Carrera, A. Barreiro, A. C. Halpern, S. Puig, J. Malvehy, Bcn20000: Dermoscopic lesions in the wild (2019). [arXiv:1908.02288](https://arxiv.org/abs/1908.02288).
- [7] P. Tschandl, C. Rosendahl, H. Kittler, The ham10000 dataset, a large collection of multi-source dermatoscopic images of common pigmented skin lesions, *Scientific Data* 5 (1) (Aug. 2018). [doi:10.1038/sdata.2018.161](https://doi.org/10.1038/sdata.2018.161).
URL <http://dx.doi.org/10.1038/sdata.2018.161>
- [8] International skin imaging collaboration (isic) archive Accessed: 2024-03-28 (2024).

- [9] C. Serrano, M. Lazo, A. Serrano, T. Toledo-Pastrana, R. Barros-Tornay, B. Acha, Clinically inspired skin lesion classification through the detection of dermoscopic criteria for basal cell carcinoma, *Journal of Imaging* 8 (7) (2022) 197.
- [10] R. R. Selvaraju, M. Cogswell, A. Das, R. Vedantam, D. Parikh, D. Batra, Grad-cam: Visual explanations from deep networks via gradient-based localization, *International Journal of Computer Vision* 128 (2) (2019) 336–359. doi:10.1007/s11263-019-01228-7.
URL <http://dx.doi.org/10.1007/s11263-019-01228-7>
- [11] B. H. van der Velden, H. J. Kuijf, K. G. Gilhuijs, M. A. Viergever, Explainable artificial intelligence (XAI) in deep learning-based medical image analysis, *Medical Image Analysis* 79 (2022) 102470. doi:10.1016/j.media.2022.102470.
URL <http://dx.doi.org/10.1016/j.media.2022.102470>
- [12] C. Barata, M. E. Celebi, J. S. Marques, Explainable skin lesion diagnosis using taxonomies, *Pattern Recognition* 110 (2021) 107413. doi:<https://doi.org/10.1016/j.patcog.2020.107413>.
URL <https://www.sciencedirect.com/science/article/pii/S0031320320302168>
- [13] T. Chanda, K. Hauser, S. Hobelsberger, T.-C. Bucher, C. N. Garcia, C. Wies, H. Kittler, P. Tschandl, C. Navarrete-Dechent, S. Podlipnik, et al., Dermatologist-like explainable ai enhances trust and confidence in diagnosing melanoma, *Nature Communications* 15 (1) (2024) 524.
- [14] E. Rezk, M. Eltorki, W. El-Dakhakhni, Interpretable skin cancer classification based on incremental domain knowledge learning, *Journal of Healthcare Informatics Research* 7 (1) (2023) 59 – 83, cited by: 4. doi:10.1007/s41666-023-00127-4.
- [15] K. Peris, E. Altobelli, A. Ferrari, M. C. Fagnoli, D. Piccolo, M. Esposito, S. Chimenti, Interobserver agreement on dermoscopic features of pigmented basal cell carcinoma, *Dermatologic surgery* 28 (7) (2002) 643–645.
- [16] S. Polesie, L. Sundback, M. Gillstedt, H. Ceder, J. D. Gyllencreutz, J. Fougelberg, E. J. Backman, J. Pakka, Z. Oscar, J. Paoli, Interobserver

- agreement on dermoscopic features and their associations with in situ and invasive cutaneous melanomas, *Acta Dermato-Venereologica* 101 (10) (2021).
- [17] A. P. Dawid, A. M. Skene, Maximum likelihood estimation of observer error-rates using the em algorithm, *Journal of the Royal Statistical Society: Series C (Applied Statistics)* 28 (1) (1979) 20–28.
- [18] F. Silva Clavería, C. Serrano, I. Matas, A. Serrano, T. Toledo-Pastrana, B. Acha, Concordance in basal cell carcinoma diagnosis. Building a proper ground truth to train CAD systems, Submitted (2024).
- [19] B. Zhou, A. Khosla, A. Lapedriza, A. Oliva, A. Torralba, Learning deep features for discriminative localization, in: 2016 IEEE Conference on Computer Vision and Pattern Recognition (CVPR), IEEE Computer Society, Los Alamitos, CA, USA, 2016, pp. 2921–2929. doi:10.1109/CVPR.2016.319.
URL <https://doi.ieeecomputersociety.org/10.1109/CVPR.2016.319>
- [20] A. Defazio, H. Mehta, K. Mishchenko, A. Khaled, A. Cutkosky, et al., The road less scheduled, arXiv preprint arXiv:2405.15682 (2024).
- [21] T. Lin, P. Goyal, R. Girshick, K. He, P. Dollar, Focal loss for dense object detection, in: 2017 IEEE International Conference on Computer Vision (ICCV), IEEE Computer Society, Los Alamitos, CA, USA, 2017, pp. 2999–3007. doi:10.1109/ICCV.2017.324.
URL <https://doi.ieeecomputersociety.org/10.1109/ICCV.2017.324>
- [22] T. Hastie, R. Tibshirani, J. Friedman, *The Elements of Statistical Learning: Data Mining, Inference, and Prediction*, Second Edition, 2nd Edition, Springer Series in Statistics, Springer New York, NY, 2009. doi:<https://doi.org/10.1007/978-0-387-84858-7>.
- [23] M. Stone, Cross-validatory choice and assessment of statistical predictions, *Journal of the Royal Statistical Society. Series B (Methodological)* 36 (2) (1974) 111–147.
URL <http://www.jstor.org/stable/2984809>

- [24] A. Krizhevsky, I. Sutskever, G. E. Hinton, Imagenet classification with deep convolutional neural networks, in: F. Pereira, C. Burges, L. Bottou, K. Weinberger (Eds.), *Advances in Neural Information Processing Systems*, Vol. 25, Curran Associates, Inc., 2012.
URL https://proceedings.neurips.cc/paper_files/paper/2012/file/c399862d3b9d6b76c8436e924a68c45b-Paper.pdf
- [25] D. Cireşan, U. Meier, J. Schmidhuber, Multi-column deep neural networks for image classification, *Proceedings / CVPR, IEEE Computer Society Conference on Computer Vision and Pattern Recognition. IEEE Computer Society Conference on Computer Vision and Pattern Recognition (02 2012)*. doi:10.1109/CVPR.2012.6248110.
- [26] P. Simard, D. Steinkraus, J. Platt, Best practices for convolutional neural networks applied to visual document analysis, in: *Seventh International Conference on Document Analysis and Recognition, 2003. Proceedings.*, 2003, pp. 958–963. doi:10.1109/ICDAR.2003.1227801.